

# Nanoscale Mapping of the Double Layer Potential at the Graphene–Electrolyte Interface

Evgheni Strelcov,\* Christopher Arble,<sup>▽</sup> Hongxuan Guo,<sup>▽</sup> Brian D. Hoskins, Alexander Yulaev, Ivan V. Vlassiuk, Nikolai B. Zhitenev, Alexander Tselev, and Andrei Kolmakov



Cite This: *Nano Lett.* 2020, 20, 1336–1344



Read Online

ACCESS |



Metrics & More



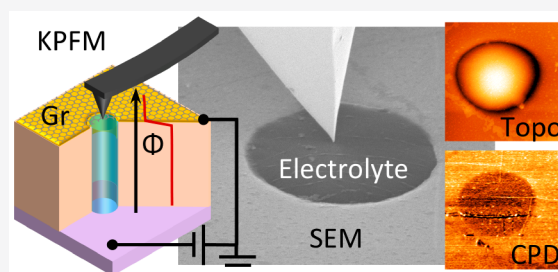
Article Recommendations



Supporting Information

**ABSTRACT:** The electrical double layer (EDL) governs the operation of multiple electrochemical devices, determines reaction potentials, and conditions ion transport through cellular membranes in living organisms. The few existing methods of EDL probing have low spatial resolution, usually only providing spatially averaged information. On the other hand, traditional Kelvin probe force microscopy (KPFM) is capable of mapping potential with nanoscale lateral resolution but cannot be used in electrolytes with concentrations higher than several mmol/L. Here, we resolve this experimental impediment by combining KPFM with graphene-capped electrolytic cells to quantitatively measure the potential drop across the EDL in aqueous electrolytes of decimolar and molar concentrations with a high lateral resolution. The surface potential of graphene in contact with deionized water and 0.1 mol/L solutions of  $\text{CuSO}_4$  and  $\text{MgSO}_4$  as a function of counter electrode voltage is reported. The measurements are supported by numerical modeling to reveal the role of the graphene membrane in potential screening and to determine the EDL potential drop. The proposed approach proves to be especially useful for imaging spatially inhomogeneous systems, such as nanoparticles submerged in an electrolyte solution. It could be suitable for in operando and in vivo measurements of the potential drop in the EDL on the surfaces of nanocatalysts and biological cells in equilibrium with liquid solutions.

**KEYWORDS:** Electrical double layer, graphene, electrolyte interface, KPFM, SEM



Electrified solid–liquid interfaces play a central role in a multitude of natural phenomena and underpin the operation of various electrochemical devices ranging from batteries and fuel cells<sup>1</sup> to supercapacitors,<sup>2</sup> electrocatalysts,<sup>3</sup> electrochromatographics,<sup>4</sup> and electrophoretic devices.<sup>5</sup> In the simplest case, interface electrification leads to the ordering of ions and solvent molecules on its surface with the formation of the electrical double layer (EDL). Although more complex phenomena including charge transport through the interface, ion desolvation, electrolysis, corrosion, and so forth are possible, the EDL by itself controls the operation of several devices, such as supercapacitors<sup>2</sup> and electric-double-layer field-effect transistors.<sup>6,7</sup> This fact necessitates a thorough understanding of the EDL behavior and properties. However, the nanoscopic length scale, inhomogeneities of the interface, localization of adsorption centers, and complexity of charge and mass transfer make it difficult to study EDLs. Even though the theoretical framework for EDL description was developed more than a century ago (Helmholtz,<sup>8</sup> later Gouy–Chapman<sup>9,10</sup> and Stern<sup>11</sup> models) and remains the foundation of the modern electrochemistry, only a limited number of experimental methods are available for measuring EDL composition and electric potential distribution.<sup>12</sup>

Traditional titration,<sup>13</sup> electrokinetic<sup>14</sup> and impedance<sup>15</sup> techniques only provide spatially averaged information on the surface charge. State of the art surface sensitive (photo)-electron and optical spectroscopy methods feature high nanometer-scale depth resolution and a few tens of nanometers lateral resolution.<sup>12,16</sup> However, most of the surface sensitive techniques require ultrahigh-vacuum-compatible samples or complex differential-pumping systems.<sup>17,18</sup> Despite these impediments, compositional variations in the EDL and its capacitance have been probed with XPS and X-ray methods in the past decade.<sup>19–22</sup> High-resolution electron imaging of the liquid–solid interface has been demonstrated only recently with the development of microchannel electrolytic cells capped with electron-transparent graphene membranes that separate the liquid electrolyte from the vacuum environment.<sup>16,23–28</sup>

Scanning ultramicroelectrode methods, such as scanning electrochemical microscopy and scanning ion conductance microscopy, are amperometric electrochemical techniques<sup>29</sup>

**Received:** November 21, 2019

**Revised:** January 22, 2020

**Published:** January 28, 2020



ACS Publications

© 2020 American Chemical Society

1336

<https://dx.doi.org/10.1021/acs.nanolett.9b04823>  
Nano Lett. 2020, 20, 1336–1344

but in principle can be used in potentiometric mode.<sup>30</sup> They have been used to probe ultrafast kinetics of short-lived species in solutions, active sites and topography of nanoparticles, and bacterial mats.<sup>29,31,32</sup> However, their lateral resolution is limited by the micropipette opening size and is typically in the micron range with a lateral resolution between 50 and 100 nm<sup>31</sup> and state-of-the-art lateral resolution of 15 nm.<sup>33</sup> Finally, atomic force microscopy (AFM) force–distance measurements have been successfully applied to both dilute aqueous electrolytes<sup>34–39</sup> and ionic liquids<sup>40–44</sup> to measure the structure of the EDL with atomic vertical and lateral resolution. Very recently, infrared nanospectroscopic AFM measurements of the graphene–electrolyte interface<sup>45</sup> and thin water layers trapped between substrate and graphene membranes<sup>46,47</sup> have been reported. There is considerable interest in determining not only the structure and composition but also the potential drop within EDL which controls the reaction kinetics. It is especially important for biomedical research, where the probing of the membrane potential of large eukaryotic cells has been routinely done since the 1960s with micropipette clamps, but methods for measuring the bacterial membrane potential have only started to be developed.<sup>48</sup> The Kelvin probe force microscopy (KPFM) AFM technique allows for the measurement of the surface potential in air or in vacuum with a very high lateral resolution (down to the atomic level) but it fails in electrolyte solutions with ionic strengths higher than a few mmol/L due to the complexity of the ion dynamics screening the tip, electrolysis, and related phenomena (see, e.g., refs 49 and 50, review in ref 51, and references therein). The same applies to other AFM methods for measuring the EDL potential with the liquid-submerged tip, such as the electric potential microscopy<sup>52–54</sup> and electrochemical force microscopy.<sup>49</sup> At the same time, electrochemical and bioapplications usually rely on electrolytes with decimolar and higher concentrations.

In this report, we combine the vacuum-compatible electrolytic cells developed recently for photoemission and electron microscopies with KPFM to probe the EDL potential drop and charge with a high lateral spatial resolution. In this setup, the AFM probe operates under vacuum and is separated from the liquid electrolyte by a graphene membrane, which eliminates the aforementioned challenges of in-liquid KPFM measurements. On the other hand, electrically conducting but very thin graphene has a limited capacity to screen the electrolyte potential and serves as a partially electrostatically transparent conducting electrode, allowing the probing of the EDL potential drop as a function of the counter-electrode bias.

Figure 1b shows a schematic of the microchannel array (MCA)<sup>16,25</sup> platform implemented here to probe the EDL potential drop. The MCA is a 400  $\mu\text{m}$  thick silicon wafer with an array of etched-through channels. The microchannels are 30  $\mu\text{m}$  in diameter on the back side, tapering to 6  $\mu\text{m}$  diameter openings on the front side. The microchannels are separated by about 45  $\mu\text{m}$  on the front side, thereby making the liquid exchange between them by surface diffusion nearly impossible. The whole MCA, including the channels' interior walls, is conformally oxidized with a 500 nm thick  $\text{SiO}_2$  insulating layer. Following oxidation, the MCA was coated with a Cr/Au (5 nm/200 nm thick, 13  $\mu\text{m}$  deep into the channel) metal film on the front side by sputtering and with Cr/Cu film (5 nm/200 nm thick, 100  $\mu\text{m}$  deep into the channel) on the back with electron beam evaporation. The front side on the MCA is covered with a bilayer graphene membrane, then the channels

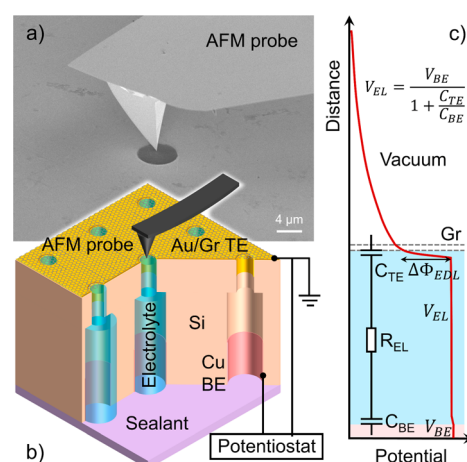


**Figure 1.** Experimental setup for probing the EDL potential drop. (a) SEM micrograph of the AFM tip in contact with a single electrolyte-filled cell. (b) A schematic of the microchannel array filled with an electrolyte. The array features a gold TE covered with a graphene membrane and a copper BE on the other side of the channels. The AFM probe is used in the KPFM mode to probe the electric potential of the graphene determined by the electrolyte underneath it as the potentiostat applies voltage to the BE. The gold/graphene TE was kept grounded at all times. (c) A schematic of potential distribution along the central axis of a single channel capped with a bilayer graphene membrane. The system's equivalent circuit includes capacitances of the EDLs at the electrodes ( $C_{TE}$  and  $C_{BE}$ ) and electrolyte resistance ( $R_{EL}$ ). The capacitance ratio determines a constant potential inside the electrolyte ( $V_{EL}$ , in the blue-shaded region), which is almost equal to the bottom electrode potential ( $V_{BE}$ , pink region). Most of this potential drops on the graphene–electrolyte interface ( $\Delta\Phi_{EDL}$ ), another portion drops in between the graphene layers, and the rest leaks into vacuum, where it is measured by KPFM.

are filled with an electrolyte and sealed on the back with a water-immiscible glue (see SI Figure S1 for details). The MCA was placed in a vacuum SEM chamber housing an AFM and was connected to a potentiostat to perform electrochemical measurements. The SEM helps with navigating the AFM tip with high precision, monitoring the sample condition over time, and performing comparative SEM/AFM imaging. The gold top electrode (TE) was kept grounded at all times for reference, and the copper bottom electrode (BE) was biased. The KPFM probe (in the amplitude-modulated tapping mode) was engaged with the graphene membrane over an individual microchannel (cell) to measure the electrostatic potential induced in the vacuum above the graphene membrane by the EDL charges (Figure 1a). The vacuum environment (residual pressure  $\approx 1 \times 10^{-4}$  Pa) ensures the cleanliness of the membrane and probe, as well as the absence of condensed water layers on them, which could additionally screen the electrolyte potential. Thus due to its unique tensile strength and high electronic conductivity, the graphene membrane acts as both an ultimately thin but robust physical barrier between the electrolyte and AFM tip, as well as an active electrode.

For a grounded conductive sample, KPFM measures the contact potential difference (CPD), the difference in the electronic work functions ( $\phi$ ) of the AFM tip and the point on the sample under the tip normalized to the elementary charge ( $e$ ):  $CPD = \frac{\phi_{tip} - \phi_{sample}}{e}$ .<sup>55</sup> Imaging the electrolyte-filled cells with the amplitude-modulated KPFM revealed that although

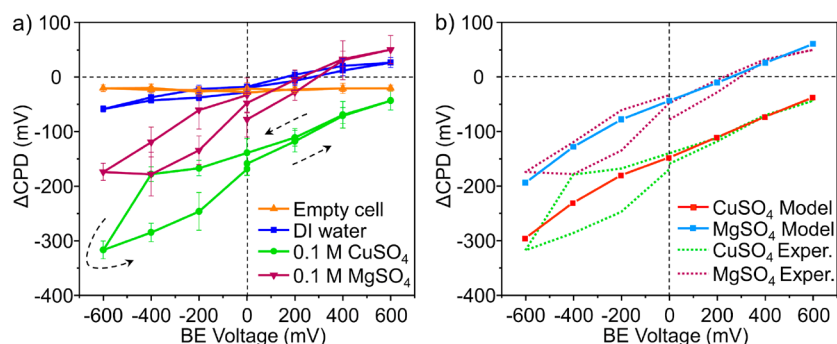


**Figure 2.** Probing the EDL potential drop: (a)  $\Delta\text{CPD}$  as a function of voltage applied to the BE for an empty cell, and cells filled with deionized water, 0.1 mol/L  $\text{CuSO}_4$ , and  $\text{MgSO}_4$  aqueous solutions. Cells were capped with bilayer graphene membranes. Points represent the average values measured over a  $1\ \mu\text{m} \times 12\ \mu\text{m}$  region encompassing cell and frame (see Figures S3 and S4, SI). The error bars represent the standard deviation of the measurements across the pixels of the area used for averaging. Dashed arrows show the voltage sweep direction. (b) Experimental data for  $\text{CuSO}_4$  and  $\text{MgSO}_4$  solutions from panel a overlaid with curves calculated with a finite-elements model.

the graphene-covered gold was grounded, the measured CPD was generally different on the cell (graphene over electrolyte) than on the neighboring MCA frame (graphene over gold). Moreover, while the CPD of the graphene-covered gold stayed nearly constant (with only some drift over time), the CPD over the electrolyte-filled cells follows the voltage applied to the BE (see SI, Figures S3 and S4). To eliminate the effect of CPD drift (due to adsorbate-induced slow changes in the tip coating's work function), we consider the change in the cell's CPD relative to the CPD of the MCA frame:  $\Delta\text{CPD} = \text{CPD}_{\text{cell}} - \text{CPD}_{\text{frame}} = -(\varphi_{\text{cell}} - \varphi_{\text{frame}})/e$ . Here, the subtraction was performed for each line of a KPFM image, as the AFM tip scanned from a cell region to frame and back (for details, see SI, Figure S3). Note that  $\Delta\text{CPD}$  is independent of the state of the tip. Spatially averaged  $\Delta\text{CPDs}$  measured on several samples including an empty cell, cells filled with deionized water, and 0.1 mol/L solutions of  $\text{CuSO}_4$  and  $\text{MgSO}_4$  (with 0.01 mol/L  $\text{H}_2\text{SO}_4$ ) are plotted in Figure 2a as a function of the BE voltage. Voltage was swept in steps of 0.2 V from 0 V to +0.6 V then to -0.6 V and back to 0 V. For the empty cell,  $\Delta\text{CPD}$  is independent of the BE voltage, confirming that the KPFM signal is not affected by the application of a voltage bias to the BE in the absence of electrolyte.  $\Delta\text{CPD}$  of a water-filled cell has a weak linear dependence on the BE bias with negligible hysteresis. Both copper and magnesium sulfate electrolyte cells displayed a strong dependence of  $\Delta\text{CPD}$  on the BE potential, and a significant hysteresis in the negative polarity region (Figure 2a). Linear dependence of  $\Delta\text{CPD}$  on the BE bias, as well as a small hysteresis, were also seen for other concentrations (e.g., Figure S10 in SI shows data for 1 mol/L  $\text{CuSO}_4$ ). We have also observed similar results with SEM, where biasing of the BE led to reversible changes in the secondary electron yield over the channel due to changes in the EDL potential drop.

Given that the bilayer graphene that capped the micro-channels in these experiments has a low density of electronic states and cannot fully screen the electric charges underneath its surface, we interpret the data of Figure 2a as a partially screened electrolyte potential measured by KPFM. To elucidate the curves in Figure 2a, first it should be noted that the electrode coatings extend into the MCA channels. For an empty cell as well as for strongly diluted electrolytes (DI water), the potential distribution inside the channel is determined by the electrode potentials and the floating potential of the conducting Si substrate (separated from the

electrode films and electrolyte by a 500 nm thick insulating layer of  $\text{SiO}_2$ ). In this case, the potential at the top of the channels is close to zero, being dominated by the grounded gold electrode film. However, in the case of a high salt concentration with a short Debye length in the electrolyte (solutions of  $\text{CuSO}_4$  and  $\text{MgSO}_4$ ), the potential is uniform across the entire electrolyte volume (except in the EDLs at its boundaries) and is determined by the EDL capacitances at the top and bottom electrodes (Figure 1c). The capacitance ratio is equal to the ratio of the metallized areas of the electrodes in contact with the electrolyte:  $\frac{100\ \mu\text{m} \times 30\ \mu\text{m}}{13\ \mu\text{m} \times 6\ \mu\text{m}} \approx 40$  for the MCA electrode geometry. Hence, the electrolyte potential ( $V_{\text{EL}}$ ) is approximately equal to the potential of the larger bottom electrode because of a significantly larger EDL capacitance at the BE:  $V_{\text{EL}} = \frac{V_{\text{BE}}}{1 + \frac{C_{\text{TE}}}{C_{\text{BE}}}} \approx 0.98V_{\text{BE}}$ , where  $V_{\text{BE}}$  is the BE voltage, and  $C_i$  are the EDL capacitances of the electrodes. The graphene membrane between vacuum and electrolyte partially screens the electrolyte potential with a potential drop across the graphene–electrolyte EDL. The unscreened portion of the potential leaks into vacuum there to be measured by the AFM probe (Figure 1c).

It is noteworthy that in Figure 2a, the  $\Delta\text{CPD}$  at zero applied bias is nonzero for all curves. The horizontal line of the empty cell is offset from zero to  $\Delta\text{CPD} \approx -22$  mV. The  $\Delta\text{CPD}$  value of the water-filled cell when the BE is grounded is about the same, whereas it is about -50 mV for the  $\text{MgSO}_4$  and -150 mV for  $\text{CuSO}_4$  solutions. We attribute these offsets to combined effects of graphene doping by contaminants during graphene growth, device fabrication, as well as by the species in the electrolyte solution. Surface doping of graphene with various chemical agents is known to significantly alter the electronic properties of this material.<sup>56</sup> For instance, the reduction of gold from aqueous solution on the graphene surface proceeds via electron transfer from graphene to gold (with the formation of a weak Au–Gr chemisorption bond) and dopes the former to become p-type:<sup>56</sup>  $\text{AuCl}_4^- + \text{Gr} + 3e^- \rightarrow \text{Au–Gr} + 4\text{Cl}^-$ . Similar doping may take place due to copper reduction in  $\text{CuSO}_4$  solution, especially under electron beam irradiation:  $\text{Cu}^{2+} + \text{Gr} + 2e^- \rightarrow \text{Cu–Gr}$ . Magnesium ions cannot be reduced in aqueous solutions to metal and are not expected to dope graphene by this mechanism. Indeed, the measured  $\Delta\text{CPD}$  shift for  $\text{MgSO}_4$  electrolyte in Figure 2a is 3 times smaller than for  $\text{CuSO}_4$ . However, doping by adsorbates



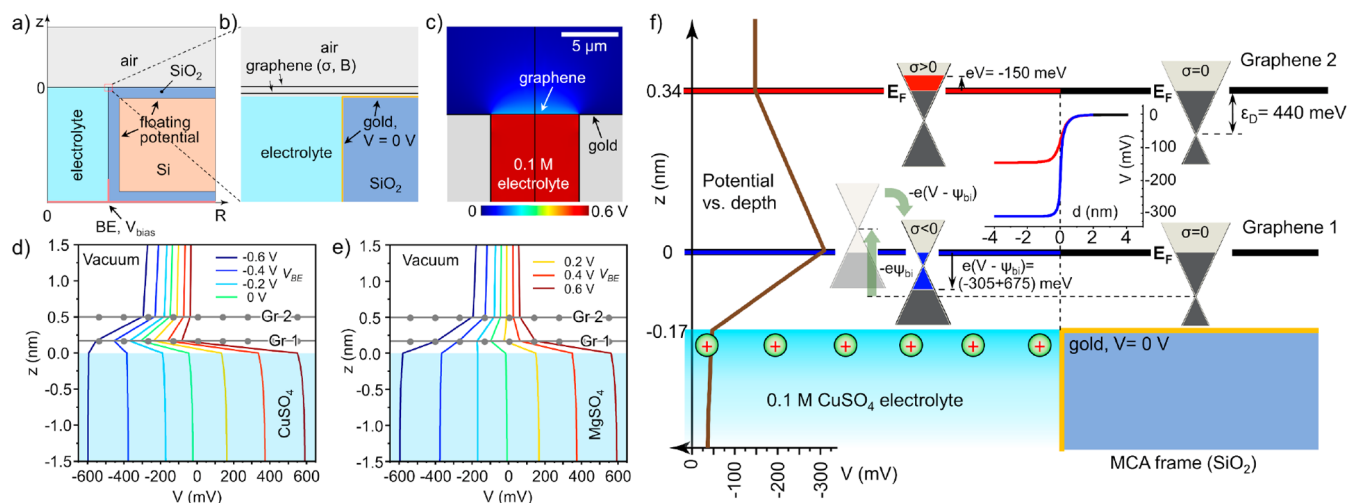


**Figure 3.** FE modeling of the potential distribution in the channels: (a) schematic of the cross-sectional channel geometry with the boundary conditions for the BE and Si matrix, (b) a zoomed-in part of (a) near the graphene–electrolyte–gold interface showing the boundary condition for the gold electrode, (c) simulated distribution map of the electric potential  $V$  in the channel and above the graphene for  $V_{BE} = +0.6$  V. (d,e) Potential distribution curves as a function of vertical distance (depth),  $z$ , for different  $V_{BE}$  for  $\text{CuSO}_4$  and  $\text{MgSO}_4$  solutions, respectively. Both graphene layers are shown. The blue-shaded rectangle indicates space filled with the electrolyte. (f) Cross-sectional schematic of an electrolyte-filled microchannel near the gold-coated wall. Two graphene layers are shown with their Dirac cones for spatial locations over gold and over electrolyte for the case of  $\text{MgSO}_4$  0.1 mol/L solution and grounded BE. The blue and red shadings within the cones illustrate the negative and positive electronic charge accumulated on the graphene layers and the corresponding amount of the band shift. The single-ended black arrows indicate the direction of the band shift under the potential difference ( $V - \psi_{bi}$ ) that leads to graphene charging at the corresponding graphene part. The shift for the bottom layer over the electrolyte can be represented as proceeding in two steps: first, the Dirac cones shift upward relative to the cones of graphene-over-gold by the built-in potential  $\psi_{bi} = -675$  mV (grayed-out cones on the left) due to doping by the electrolyte and then downward by the amount  $-e(V - \psi_{bi}) = -370$  meV (cones on the right with blue shading) due to the external ionic and electronic charge redistribution in response to the doping-induced potential. These two steps are indicated with wide green arrows. The brown curve depicts the electric potential,  $V$ , versus depth,  $z$ , dependence. The inset displays lateral potential  $V$  distributions in both of the graphene layers in the vicinity of the channel wall.

other than metallic nanoparticles could take place, for example, by products of hydrolysis:  $\text{Mg}_2(\text{OH})_2\text{SO}_4$ ,  $\text{Mg}(\text{OH})_2$ , or various products of electrolyte radiolysis and electrolysis, such as  $\text{SO}_2$ , sulfides, and mercapto-compounds.<sup>57,58</sup>

Overall, the measured local  $\Delta\text{CPD}$  at zero bias is the potential of the top graphene layer determined by two factors: induced charges in the graphene–electrolyte EDL and the shift of the Fermi level with respect to its position over the MCA frame due to alteration in the doping (see Figure 3f schematic). Solely due to a change in the doping level, the corresponding component of  $\Delta\text{CPD}$  is equal to the built-in potential,  $\psi_{bi}$ , of the p-n-like junction formed in the graphene along the channel-frame boundary due to the difference in the doping levels in the cell and frame parts of the graphene<sup>59</sup> (see Figure S5, SI, for details). This  $\Delta\text{CPD}$  is measured in the case of an empty cell (the graphene on the MCA frame can be doped by the gold underneath it).<sup>60</sup> When the electrolyte is present under graphene, the built-in potential leads to accumulation of ionic charge on the interface and some screening charge in the graphene. Additionally, accumulation of ionic charge due to adsorption and chemical interactions between the electrolyte species and graphene is possible. Therefore, an EDL will form at the electrolyte–graphene interface even at zero BE bias voltage, and the graphene layer over the cell will carry a nonzero electronic charge. Then, the  $\Delta\text{CPD}$  is a combination of  $\psi_{bi}$  and the electrostatic potential due to the induced electric charges in the EDL. Upon application of a voltage bias to the BE, the detected potential changes by the value of the unshielded portion of the electrolyte potential. The hysteresis seen in the  $\text{CuSO}_4$  and  $\text{MgSO}_4$  curves of Figure 2a in the cathodic (anodic for the TE)

regime may be due to varying the doping level presumably by electrolytic graphene oxidation.

To quantify the observed response of the MCA–graphene system to the application of a voltage bias to the BE and to relate the response to the EDL potential drop, we used finite element (FE) modeling. The FE model simulates distributions of the electric potential and ionic concentrations in the MCA–graphene system for different electrolyte strengths and potentials at the BE and relies on the Gouy–Chapman model of the EDL. For a description of the charge screening by the two-layer graphene in the direction normal to the graphene layers, we adapted the model developed by Kuroda et al.<sup>61</sup> with a doping-dependent position of the Fermi level in the graphene layers with respect to the graphene Dirac point. The model assumes an idealized situation when the graphene layers are uncoupled and the linear electron dispersion at the Dirac point of the layers is preserved. A schematic of the FE model layout is displayed in Figure 3a,b,f. In the FE model, graphene layers are represented by two boundaries of two similar dielectric domains stacked one on top of the other. The boundaries are separated by 0.34 nm, the interlayer distance of the multilayer graphene. The inner graphene layer is separated from the electrolyte and the MCA frame by half of this distance, that is, 0.17 nm. To account for the built-in potential due to doping, the surface charge density and the band-filling energy of graphene layers are calculated as functions of the difference of the electric,  $V$ , and built-in,  $\psi_{bi}$ , potentials ( $V - \psi_{bi}$ ) along the boundaries representing the graphene layers over the cell channel, which yields zero charge at  $V = \psi_{bi}$ . Figure 3c shows a simulated potential distribution map near the cell top for a channel filled with a 0.1 mol/L electrolyte solution. The map

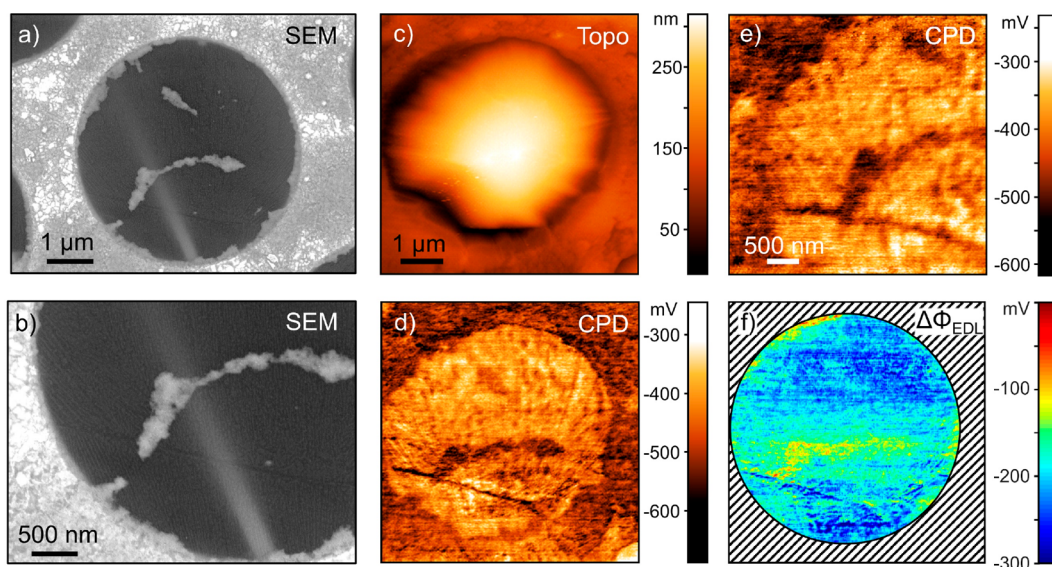


**Figure 4.** Probing an inhomogeneous system: alumina nanoparticles submerged in 0.1 mol/L  $\text{CuSO}_4$  solution and attached to a monolayer graphene membrane. (a,b) SEM images of a single electrolyte-filled cell capped with alumina-decorated graphene (nanoparticles face the electrolyte). Nanoparticles are white bumpy aggregates. (c) AFM topographic map of the same cell shows no particles on the surface of graphene facing the vacuum half-space. (d) Corresponding KPFM CPD map displays a significant contrast between the electrolyte and nanoparticles. In addition, a graphene line defect, barely visible in SEM and topographic images, can be seen crossing the lower part of these images. Topographic and CPD maps of panels c and d were recorded simultaneously. (e) CPD map of a region around the arched nanoparticle agglomerate. Graphene–gold top and copper bottom electrodes were grounded. (f) Calculated EDL potential drop map of the same cell when a  $-0.3$  V bias was applied to the BE. The shaded area is the MCA frame, circular opening is the cell. Nanoparticle aggregates at the center and on the cell periphery have smaller  $\Delta\Phi_{\text{EDL}}$  than the graphene membrane. Scale bar for panels c, d, and f is the same.

clearly reveals the unscreened potential in vacuum just above the graphene over the cell. More details on the FE model structure, verification, and examples of the calculated potential distributions can be found in SI.

To determine the EDL potential drop in the case of bilayer graphene membrane, the FE model allows the estimation of the graphene doping levels, both fabrication-related and due to the contact with an electrolyte. For that,  $\epsilon_D$ , the Fermi level shift from the Dirac point due to the fabrication-related chemical doping, and  $\psi_{\text{bi}}$  are treated as adjustable variables to closely reproduce the experimental  $\Delta\text{CPD}$  versus BE bias curves. In the general case, their values should be considered different for the two graphene layers in the bilayer graphene. However, no significant difference in the fabrication-related doping is expected for the bottom and top layers of the graphene membrane, and we have neglected this difference. Furthermore, we assume that only the inner graphene layer in contact with the electrolyte undergoes doping by electrolyte species, and  $\psi_{\text{bi}} = 0$  for the outer layer. In this case,  $\Delta\text{CPD}$  at zero applied bias is mainly controlled by  $\psi_{\text{bi}}$  of the inner layer. The slope of the  $\Delta\text{CPD}$  versus bias curve reflects the strength of the screening by the graphene membrane of the electrolyte potential: the larger the slope, the weaker the screening. A larger slope indicates a smaller density of the states at the graphene Fermi layer and, hence, a smaller net doping (i.e., net doping for DI water is larger than for sulfate electrolytes, because the latter induce doping compensation; see next paragraph). These considerations provide guidelines for the direction and value of  $\epsilon_D$  and  $\psi_{\text{bi}}$  adjustments.

Figure 2b shows both the experimental data and simulated curves of the  $\Delta\text{CPD}$  versus bias dependence for 0.1 M  $\text{CuSO}_4$  and  $\text{MgSO}_4$  solutions. The calculated curves reproduce well the experimental data for the positive bias branch of the data. It is noteworthy that the data for  $\text{CuSO}_4$  and  $\text{MgSO}_4$  were both

fit with the same value of  $\epsilon_D = 440$  meV, corresponding to n-doping at a level of  $1.4 \times 10^{13} \text{ cm}^{-2}$  (consistent with doping in our previous report<sup>62</sup>). With p-doping, the anodic behavior of the experimental curves could not be reproduced; a noticeable positive curvature of the plot lines would be expected in this case due to approach of the Dirac point by the Fermi level upon application of the positive BE bias, whereas the experimental data instead indicate a negative curvature of the cathodic branch. The calculated  $\psi_{\text{bi}} = -675$  mV for  $\text{CuSO}_4$  and  $-240$  mV for  $\text{MgSO}_4$ , which yields, respectively,  $4.1 \times 10^{12} \text{ cm}^{-2}$  p-type net doping and  $2.9 \times 10^{12} \text{ cm}^{-2}$  n-type net doping for the inner graphene layer in contact with electrolytes. Both electrolytes effectively dope graphene p-type (doping compensation) with the doping level changes of about  $1.8 \times 10^{13} \text{ cm}^{-2}$  for  $\text{CuSO}_4$  and  $1.1 \times 10^{13}$  for  $\text{MgSO}_4$ . Figure 3f displays a band structure diagram for graphene layers corresponding to the calculated potential distribution at zero BE bias for the  $\text{MgSO}_4$  solution. The measured negative  $\Delta\text{CPD}$  at zero BE bias can be interpreted as arising due to the built-in potential of the inner graphene layer. This potential is partially screened by the positive charges on the top graphene layer and in the EDL of the electrolyte. Figure 3d,e displays potential profiles in the vicinity of the graphene membrane along the cell channel axis (depth) for BE bias values used in the KPFM experiments. The value of the built-in potential is comparable to the maximal value of the applied BE bias, and its effect on the behavior of the potential across the EDL and graphene is pronounced, which should be accounted for when using the KPFM-measured potential to determine the EDL potential drop.

The proposed method of probing the EDL with KPFM through the graphene membrane could prove most useful for spatially inhomogeneous systems, such as electrocatalytic or biological ones. The surface of nanoobjects (catalysts or

biocells) residing on graphene and submerged in electrolyte localizes redox reactions and could be imaged as a function of an external voltage that controls which reaction is activated. As a model example of such a system, Figure 4 shows images of a microchannel capped with graphene decorated with alumina nanoparticles. For this experiment, to improve the KPFM contrast we used a monolayer graphene membrane, which yields a weaker screening compared to the bilayer graphene, and high-lateral-resolution frequency-modulated KPFM (see SI Figure S8 for details). With the monolayer graphene, the EDL potential drop at the graphene is equal to the difference between the electrolyte potential  $V_{\text{EL}}$  and the potential on the graphene. The implemented FM-KPFM featured a lateral resolution of about 20–40 nm. Nanoparticles were deposited onto a monolayer graphene membrane before filling the MCA with electrolyte, such that the nanoparticle-covered side faced the electrolyte. The graphene-surface-facing vacuum had no particles on it. The MCA was filled with a 0.1 mol/L  $\text{CuSO}_4$  solution. Figure 4a,b shows SEM images of a microchannel with nanoparticle agglomerates on the periphery and in a large arc at the cell's center. Also visible is a line defect in the graphene (a thin black line crossing the arc on the left). Topographic image of the same cell (Figure 4c) does not show any evidence of particles or line defects but does reveal the folds and overall shape of the membrane. The CPD maps (Figure 4d,e), on the other hand, show a rich pattern of nanodefects/wrinkles on the membrane, including the line defect, as well as a high-contrast image of the nanoparticle agglomerates under the graphene surface. Biasing the copper BE at negative polarity increased the contrast between the particles and the graphene membrane and decreased it at positive polarity (see SI, Figure S9). With the monolayer graphene, the EDL potential drop can be calculated as  $\Delta\Phi_{\text{EDL}} = V_{\text{EL}} - (\text{CPD}_{\text{V}} - \text{CPD}_0)$ , where  $\text{CPD}_{\text{V}}$  and  $\text{CPD}_0$  are the CPD values measured on the cell when the BE is biased and grounded, respectively. Figure 4f shows a calculated  $\Delta\Phi_{\text{EDL}}$  map for the same cell as discussed above, when a  $-0.3$  V bias was applied to the BE. Larger absolute values of  $\Delta\Phi_{\text{EDL}}$  indicate stronger screening of the electrolyte potential. The  $\Delta\Phi_{\text{EDL}}$  values approach  $-300$  mV on the clean membrane regions, especially, on the line defect but are much smaller over the nanoparticles aggregates, where hot spots and complex structures are seen. Radial wrinkles visible in the  $\text{CPD}_0$  map of Figure 4d are also absent from the  $\Delta\Phi_{\text{EDL}}$  map, indicating that such defect structure is not affecting the measurements.

More precise understanding and quantification of the CPD map contrast between the nanoparticles and electrolyte requires a thorough knowledge of the system's geometry, including the particles size, packing density in the agglomerates, deposit thickness, and presence of electrolyte between the nanoparticles and graphene membrane (see SI). When these parameters are well-controlled and no gap exists between the object of interest and the 2D membrane, ionic charge adsorbed on the object's surface will create a potential outside the membrane. We note that the use of insulating 2D materials' membranes (e.g., hexagonal boron nitride) for MCA capping will eliminate membrane-induced screening and allow for direct mapping of unscreened potential (in contrast to  $\Delta\Phi_{\text{EDL}}$ ). This potential, recorded by KPFM, in principle can be converted into the surface charge density with a high lateral resolution to reveal active adsorption/reaction sites on the nanoparticle. The limitation of the insulating membranes is that they cannot be used as active electrodes. On the other

hand, from the results reported here, it is apparent that the use of graphene membranes demands good control over the doping level of graphene for accurate determination of the EDL voltage drops. At the same time, the use of graphene with varying doping levels, and hence different densities of electronic states at the Fermi level, can provide an additional degree of freedom in the probing of the EDLs through the graphene membranes. While the use of bilayer graphene requires complex modeling to extract the  $\Delta\Phi_{\text{EDL}}$  values, the case of monolayer graphene is much simpler, allowing direct conversion of the experimental data into  $\Delta\Phi_{\text{EDL}}$  maps. Finally, a combination of KPFM and nanospectroscopy could unravel both the potential drop and chemical composition of the EDL with high lateral resolution on nano- and microscopic objects.

## CONCLUSIONS

We have demonstrated a method of quantitative measurement of the local EDL potential drop at the graphene–electrolyte interface in decimolar solutions using KPFM. A microchannel array filled with an electrolyte of choice, capped with a graphene membrane and sealed on the back can be used as a vacuum-compatible electrochemical cell. The robust and electronically conductive graphene membrane serves as an electrode and an electric-field permeable barrier that separates the AFM tip from the liquid, allowing the EDL potential to be measured. A comparison of a numerical simulation to the experiment reveals that the parameters of the graphene membrane determine the degree of screening and have to be controlled well. We also demonstrate imaging of an inhomogeneous system, where electrolyte-submerged nanoparticles residing beneath the graphene surface can be imaged with KPFM and are responsive to the externally applied bias. This method could be very useful for probing electrochemical processes on the surface of nanocatalysts and biological cells in equilibrium with liquid environments. We envision in operando measurements of the distribution of active sites within individual nanocatalytic particles and in vivo mapping of the membrane potential of individual bacterial ion channels. This could be possible provided that the nanoobject potential is not disturbed by the 2D encapsulating membrane (as in the case of an insulating membrane) and if the gap between the nanoobject and this membrane is less than the screening length of the electrolyte. Combined with nanospectroscopy and other techniques, the through-membrane KPFM approach can yield both functional and chemical information about the surface processes in liquids of high ionic strengths, as well as help refine the EDL structure.

## ASSOCIATED CONTENT

### Supporting Information

The Supporting Information is available free of charge at <https://pubs.acs.org/doi/10.1021/acs.nanolett.9b04823>.

Details on the MCA nanofabrication and characterization, data processing for Figure 2a, FE modeling, inhomogeneous system imaging, and 1 mol/L  $\text{CuSO}_4$  solution measurements (PDF)

## AUTHOR INFORMATION

### Corresponding Author

Evgheni Strelcov — Physical Measurement Laboratory, National Institute of Standards and Technology, Gaithersburg, Maryland 20899, United States; Maryland NanoCenter, University of



Maryland, College Park, Maryland 20742, United States;  
✉ [orcid.org/0000-0002-8561-3847](https://orcid.org/0000-0002-8561-3847);  
Email: [evgheni.strelcov@nist.gov](mailto:evgheni.strelcov@nist.gov)

## Authors

**Christopher Arble** – Physical Measurement Laboratory,  
National Institute of Standards and Technology, Gaithersburg,  
Maryland 20899, United States

**Hongxuan Guo** – SEU-FEI Nano-Pico Center, Key Laboratory  
of MEMS of Ministry of Education, Southeast University,  
Nanjing 210096, China; ✉ [orcid.org/0000-0002-8092-8057](https://orcid.org/0000-0002-8092-8057)

**Brian D. Hoskins** – Physical Measurement Laboratory,  
National Institute of Standards and Technology, Gaithersburg,  
Maryland 20899, United States

**Alexander Yulaev** – Physical Measurement Laboratory,  
National Institute of Standards and Technology, Gaithersburg,  
Maryland 20899, United States; Department of Chemistry and  
Biochemistry, University of Maryland, College Park, Maryland  
20742, United States; ✉ [orcid.org/0000-0002-9225-3448](https://orcid.org/0000-0002-9225-3448)

**Ivan V. Vlassiouk** – Oak Ridge National Laboratory, Oak  
Ridge, Tennessee 37830, United States; ✉ [orcid.org/0000-0002-5494-0386](https://orcid.org/0000-0002-5494-0386)

**Nikolai B. Zhitenov** – Physical Measurement Laboratory,  
National Institute of Standards and Technology, Gaithersburg,  
Maryland 20899, United States

**Alexander Tselev** – Department of Physics and  
CICECO–Aveiro Institute of Materials, University of Aveiro,  
3810-193 Aveiro, Portugal; ✉ [orcid.org/0000-0002-0098-6696](https://orcid.org/0000-0002-0098-6696)

**Andrei Kolmakov** – Physical Measurement Laboratory,  
National Institute of Standards and Technology, Gaithersburg,  
Maryland 20899, United States; ✉ [orcid.org/0000-0001-5299-4121](https://orcid.org/0000-0001-5299-4121)

Complete contact information is available at:  
<https://pubs.acs.org/10.1021/acs.nanolett.9b04823>

## Author Contributions

E.S. conceived the idea, performed the KPFM measurements, and analyzed the results. C.A. and H.G. prepared the samples. B.H. fabricated the MCA platform. I.V. fabricated graphene. A.T. performed the numerical simulations. A.K. supervised the project. The manuscript was written through contributions of all authors. All authors have given approval to the final version of the manuscript.

## Author Contributions

<sup>†</sup>C.A. and H.G. contributed equally.

## Notes

The authors declare no competing financial interest.

## ACKNOWLEDGMENTS

E.S. and H.G. acknowledge support under the Cooperative Research Agreement between the University of Maryland and the National Institute of Standards and Technology Center for Nanoscale Science and Technology, Award 70NANB14H209, through the University of Maryland. H.G. acknowledges support under the National Natural Science Foundation of China (Grant 11874105). A.Y. acknowledges support under the Professional Research Experience Program (PREP), administered through the Department of Chemistry and Biochemistry UMD. In part (A.T.), this work was developed within the scope of the project CICECO-Aveiro Institute of Materials, UIDB/50011/2020 and UIDP/50011/2020, fi-

nanced by national funds through the FCT/MEC and, when appropriate, cofinanced by FEDER under the PT2020 Partnership Agreement. E.S. would like to thank Dr. Jabez McClelland for providing access to the AFM/SEM instrument, useful discussions, and a thorough reading of the manuscript.

## ABBREVIATIONS

MCA, microchannel array; EDL, electrical double layer; AFM, atomic force microscopy; KPFM, Kelvin probe force microscopy; SEM, scanning electron microscopy

## REFERENCES

- (1) Bagotsky, V. S. *Fundamentals of Electrochemistry*; John Wiley & Sons, Inc.: Hoboken, NJ, 2005.
- (2) Yan, J.; Wang, Q.; Wei, T.; Fan, Z. J. Recent Advances in Design and Fabrication of Electrochemical Supercapacitors with High Energy Densities. *Adv. Energy Mater.* **2014**, *4*, 1300816.
- (3) Spendelov, J. S.; Wieckowski, A. Electrocatalysis of oxygen reduction and small alcohol oxidation in alkaline media. *Phys. Chem. Chem. Phys.* **2007**, *9*, 2654–2675.
- (4) Strain, H. H.; Sullivan, J. C. Analysis by Electromigration plus Chromatography. *Anal. Chem.* **1951**, *23*, 816–823.
- (5) Hunter, R. J. *Foundations of Colloid Science*; Oxford University Press: Oxford, 2001.
- (6) Yuan, H.; Shimotani, H.; Tsukazaki, A.; Ohtomo, A.; Kawasaki, M.; Iwasa, Y. High-Density Carrier Accumulation in ZnO Field-Effect Transistors Gated by Electric Double Layers of Ionic Liquids. *Adv. Funct. Mater.* **2009**, *19*, 1046–1053.
- (7) Fujimoto, T.; Awaga, K. Electric-double-layer field-effect transistors with ionic liquids. *Phys. Chem. Chem. Phys.* **2013**, *15*, 8983–9006.
- (8) Helmholtz, H. Studien über electrische Grenzschichten. *Ann. Phys. (Berlin, Ger.)* **1879**, *243*, 337–382.
- (9) Gouy, M. G. Sur la constitution de la charge électrique à la surface d'un électrolyte. *J. Phys. Theor. Appl.* **1910**, *9*, 457–468.
- (10) Chapman, D. L. A contribution to the theory of electrocapillarity. *London Edinb. Dubl. Philos. Mag.* **1913**, *25*, 475–481.
- (11) Stern, O. The Theory of the Electrolytic Double Shift. *Z. Elektrochem. Angew. P.* **1924**, *30*, 508–516.
- (12) Zaera, F. Probing Liquid/Solid Interfaces at the Molecular Level. *Chem. Rev.* **2012**, *112*, 2920–2986.
- (13) Kosmulski, M. *Surface Charging and Points of Zero Charge*; CRC Press: Boca Raton, FL, 2009.
- (14) Glawdel, T.; Ren, C. Zeta Potential Measurement. In *Encyclopedia of Microfluidics and Nanofluidics*; Li, D., Ed.; Springer: Boston, MA, 2008; pp 2199–2207.
- (15) Nam, K.-M.; Chang, B.-Y. Electrochemical Impedance Method to Measure the Potential of the Outer Helmholtz Plane. *J. Electrochem. Soc.* **2014**, *161*, H379–H383.
- (16) Guo, H.; Strelcov, E.; Yulaev, A.; Wang, J.; Appathurai, N.; Urquhart, S.; Vinson, J.; Sahu, S.; Zwolak, M.; Kolmakov, A. Enabling Photoemission Electron Microscopy in Liquids via Graphene-Capped Microchannel Arrays. *Nano Lett.* **2017**, *17*, 1034–1041.
- (17) Siegbahn, H. Electron spectroscopy for chemical analysis of liquids and solutions. *J. Phys. Chem.* **1985**, *89*, 897–909.
- (18) Salmeron, M.; Schlögl, R. Ambient pressure photoelectron spectroscopy: A new tool for surface science and nanotechnology. *Surf. Sci. Rep.* **2008**, *63*, 169–199.
- (19) Ottosson, N.; Faubel, M.; Bradforth, S. E.; Jungwirth, P.; Winter, B. Photoelectron spectroscopy of liquid water and aqueous solution: Electron effective attenuation lengths and emission-angle anisotropy. *J. Electron Spectrosc. Relat. Phenom.* **2010**, *177*, 60–70.
- (20) Brown, M. A.; Abbas, Z.; Kleibert, A.; Green, R. G.; Goel, A.; May, S.; Squires, T. M. Determination of Surface Potential and Electrical Double-Layer Structure at the Aqueous Electrolyte-Nanoparticle Interface. *Phys. Rev. X* **2016**, *6*, 011007.

- (21) Favaro, M.; Jeong, B.; Ross, P. N.; Yano, J.; Hussain, Z.; Liu, Z.; Crumlin, E. J. Unravelling the electrochemical double layer by direct probing of the solid/liquid interface. *Nat. Commun.* **2016**, *7*, 12695.
- (22) Bourg, I. C.; Lee, S. S.; Fenter, P.; Tournassat, C. Stern Layer Structure and Energetics at Mica–Water Interfaces. *J. Phys. Chem. C* **2017**, *121*, 9402–9412.
- (23) Kolmakov, A.; Dikin, D. A.; Cote, L. J.; Huang, J.; Abyaneh, M. K.; Amati, M.; Gregoratti, L.; Gunther, S.; Kiskinova, M. Graphene oxide windows for in situ environmental cell photoelectron spectroscopy. *Nat. Nanotechnol.* **2011**, *6*, 651–657.
- (24) Nemšák, S.; Strelcov, E.; Duchoň, T.; Guo, H.; Hackl, J.; Yulaev, A.; Vlassioux, I.; Mueller, D. N.; Schneider, C. M.; Kolmakov, A. Interfacial Electrochemistry in Liquids Probed with Photoemission Electron Microscopy. *J. Am. Chem. Soc.* **2017**, *139*, 18138–18141.
- (25) Yulaev, A.; Guo, H.; Strelcov, E.; Chen, L.; Vlassioux, I.; Kolmakov, A. Graphene Microcapsule Arrays for Combinatorial Electron Microscopy and Spectroscopy in Liquids. *ACS Appl. Mater. Interfaces* **2017**, *9*, 26492–26502.
- (26) Stoll, J. D.; Kolmakov, A. Electron Transparent Graphene Windows for Environmental Scanning Electron Microscopy in Liquids and Dense Gases. *Nanotechnology* **2012**, *23*, S05704.
- (27) Velasco-Velez, J. J.; Pfeifer, V.; Hävecker, M.; Weatherup, R. S.; Arrigo, R.; Chuang, C.-H.; Stotz, E.; Weinberg, G.; Salmeron, M.; Schlögl, R.; Knop-Gericke, A. Photoelectron Spectroscopy at the Graphene–Liquid Interface Reveals the Electronic Structure of an Electrodeposited Cobalt/Graphene Electrocatalyst. *Angew. Chem., Int. Ed.* **2015**, *54*, 14554–14558.
- (28) Weatherup, R. S.; Eren, B.; Hao, Y.; Bluhm, H.; Salmeron, M. B. Graphene Membranes for Atmospheric Pressure Photoelectron Spectroscopy. *J. Phys. Chem. Lett.* **2016**, *7*, 1622–1627.
- (29) Bentley, C. L.; Edmondson, J.; Meloni, G. N.; Perry, D.; Shkirskiy, V.; Unwin, P. R. Nanoscale Electrochemical Mapping. *Anal. Chem.* **2019**, *91*, 84–108.
- (30) Zhou, Y.; Chen, C.-C.; Weber, A. E.; Zhou, L.; Baker, L. A.; Hou, J. Potentiometric-scanning ion conductance microscopy for measurement at tight junctions. *Tissue Barriers* **2013**, *1*, e25585–e25585.
- (31) Kai, T.; Zoski, C. G.; Bard, A. J. Scanning Electrochemical Microscopy at the Nanometer Level. *Chem. Commun.* **2018**, *54*, 1934–1947.
- (32) Conzuelo, F.; Schulte, A.; Schuhmann, W. Biological imaging with scanning electrochemical microscopy. *Proc. R. Soc. London, Ser. A* **2018**, *474*, 20180409.
- (33) Sun, T.; Wang, D.; Mirkin, M. V.; Cheng, H.; Zheng, J.-C.; Richards, R. M.; Lin, F.; Xin, H. L. Direct high-resolution mapping of electrocatalytic activity of semi-two-dimensional catalysts with single-edge sensitivity. *Proc. Natl. Acad. Sci. U. S. A.* **2019**, *116*, 201821091.
- (34) Siretanu, I.; Ebeling, D.; Andersson, M. P.; Stipp, S. L. S.; Philipse, A.; Stuart, M. C.; van den Ende, D.; Mugele, F. Direct observation of ionic structure at solid-liquid interfaces: a deep look into the Stern Layer. *Sci. Rep.* **2015**, *4*, 4956.
- (35) Zhao, C.; Ebeling, D.; Siretanu, I.; van den Ende, D.; Mugele, F. Extracting local surface charges and charge regulation behavior from atomic force microscopy measurements at heterogeneous solid-electrolyte interfaces. *Nanoscale* **2015**, *7*, 16298–16311.
- (36) Ebeling, D.; van den Ende, D.; Mugele, F. Electrostatic interaction forces in aqueous salt solutions of variable concentration and valency. *Nanotechnology* **2011**, *22*, 305706.
- (37) Martin-Jimenez, D.; Chacon, E.; Tarazona, P.; Garcia, R. Atomically resolved three-dimensional structures of electrolyte aqueous solutions near a solid surface. *Nat. Commun.* **2016**, *7*, 12164.
- (38) Ricci, M.; Spijker, P.; Voitchovsky, K. Water-induced correlation between single ions imaged at the solid–liquid interface. *Nat. Commun.* **2014**, *5*, 4400.
- (39) Hofmann, S.; Voitchovsky, K.; Spijker, P.; Schmidt, M.; Stumpf, T. Visualising the molecular alteration of the calcite (104)–water interface by sodium nitrate. *Sci. Rep.* **2016**, *6*, 21576.
- (40) Atkin, R.; El Abedin, S. Z.; Hayes, R.; Gasparotto, L. H. S.; Borisenko, N.; Endres, F. AFM and STM Studies on the Surface Interaction of [BMP]TfSA and [EMIm]TfSA Ionic Liquids with Au(111). *J. Phys. Chem. C* **2009**, *113*, 13266–13272.
- (41) Hayes, R.; Borisenko, N.; Tam, M. K.; Howlett, P. C.; Endres, F.; Atkin, R. Double Layer Structure of Ionic Liquids at the Au(111) Electrode Interface: An Atomic Force Microscopy Investigation. *J. Phys. Chem. C* **2011**, *115*, 6855–6863.
- (42) Black, J. M.; Walters, D.; Labuda, A.; Feng, G.; Hillesheim, P. C.; Dai, S.; Cummings, P. T.; Kalinin, S. V.; Proksch, R.; Balke, N. Bias-Dependent Molecular-Level Structure of Electrical Double Layer in Ionic Liquid on Graphite. *Nano Lett.* **2013**, *13*, S954–S960.
- (43) Black, J. M.; Baris Okatan, M.; Feng, G.; Cummings, P. T.; Kalinin, S. V.; Balke, N. Topological Defects in Electric Double Layers of Ionic Liquids at Carbon Interfaces. *Nano Energy* **2015**, *15*, 737–745.
- (44) Tsai, W.-Y.; Come, J.; Zhao, W.; Wang, R.; Feng, G.; Prasad Thapaliya, B.; Dai, S.; Collins, L.; Balke, N. Hysteretic order-disorder transitions of ionic liquid double layer structure on graphite. *Nano Energy* **2019**, *60*, 886–893.
- (45) Lu, Y.-H.; Larson, J. M.; Baskin, A.; Zhao, X.; Ashby, P. D.; Prendergast, D.; Bechtel, H. A.; Kostecky, R.; Salmeron, M. Infrared Nanospectroscopy at the Graphene–Electrolyte Interface. *Nano Lett.* **2019**, *19*, 5388–5393.
- (46) Hong, Y.; Wang, S.; Li, Q.; Song, X.; Wang, Z.; Zhang, X.; Besenbacher, F.; Dong, M. Interfacial Icelike Water Local Doping of Graphene. *Nanoscale* **2019**, *11*, 19334–19340.
- (47) Khatib, O.; Wood, J. D.; McLeod, A. S.; Goldflam, M. D.; Wagner, M.; Damhorst, G. L.; Koepke, J. C.; Doidge, G. P.; Rangarajan, A.; Bashir, R.; Pop, E.; Lyding, J. W.; Thiemens, M. H.; Keilmann, F.; Basov, D. N. Graphene-Based Platform for Infrared Near-Field Nanospectroscopy of Water and Biological Materials in an Aqueous Environment. *ACS Nano* **2015**, *9*, 7968–7975.
- (48) Stratford, J. P.; Edwards, C. L. A.; Ghanshyam, M. J.; Malyshev, D.; Delise, M. A.; Hayashi, Y.; Asally, M. Electrically induced bacterial membrane-potential dynamics correspond to cellular proliferation capacity. *Proc. Natl. Acad. Sci. U. S. A.* **2019**, *116*, 9552–9557.
- (49) Collins, L.; Jesse, S.; Kilpatrick, J. I.; Tselev, A.; Varenky, O.; Okatan, M. B.; Weber, S. A. L.; Kumar, A.; Balke, N.; Kalinin, S. V.; Rodriguez, B. J. Probing Charge Screening Dynamics and Electrochemical Processes at the Solid–Liquid Interface with Electrochemical Force Microscopy. *Nat. Commun.* **2014**, *5*, 3871.
- (50) Collins, L.; Kilpatrick, J. I.; Vlassioux, I. V.; Tselev, A.; Weber, S. A. L.; Jesse, S.; Kalinin, S. V.; Rodriguez, B. J. Dual Harmonic Kelvin Probe Force Microscopy at the Graphene–Liquid Interface. *Appl. Phys. Lett.* **2014**, *104*, 133103.
- (51) Collins, L.; Kilpatrick, J. I.; Kalinin, S. V.; Rodriguez, B. J. Towards nanoscale electrical measurements in liquid by advanced KPFM techniques: a review. *Rep. Prog. Phys.* **2018**, *81*, 086101.
- (52) Kobayashi, N.; Asakawa, H.; Fukuma, T. Quantitative potential measurements of nanoparticles with different surface charges in liquid by open-loop electric potential microscopy. *J. Appl. Phys.* **2011**, *110*, 044315.
- (53) Kobayashi, N.; Asakawa, H.; Fukuma, T. Dual frequency open-loop electric potential microscopy for local potential measurements in electrolyte solution with high ionic strength. *Rev. Sci. Instrum.* **2012**, *83*, 033709.
- (54) Hirata, K.; Kitagawa, T.; Miyazawa, K.; Okamoto, T.; Fukunaga, A.; Takato, C.; Fukuma, T. Visualizing charges accumulated in an electric double layer by three-dimensional open-loop electric potential microscopy. *Nanoscale* **2018**, *10*, 14736–14746.
- (55) Melitz, W.; Shen, J.; Kummel, A. C.; Lee, S. Kelvin Probe Force Microscopy and its Application. *Surf. Sci. Rep.* **2011**, *66*, 1–27.
- (56) Lee, H.; Paeng, K.; Kim, I. S. A review of doping modulation in graphene. *Synth. Met.* **2018**, *244*, 36–47.
- (57) Loeffler, M. J.; Hudson, R. L.; Moore, M. H.; Carlson, R. W. Radiolysis of sulfuric acid, sulfuric acid monohydrate, and sulfuric acid tetrahydrate and its relevance to Europa. *Icarus* **2011**, *215*, 370–380.



- (58) Tenchurina, A. R.; Sal'keeva, A. K. Radiolysis and photolysis of sodium sulfate crystalline hydrate. *Russ. J. Phys. Chem. A* **2016**, *90*, 688–690.
- (59) Sze, S. M. *Physics of Semiconductor Devices*, second ed.; John Wiley & Sons: New York, 1981; p 868.
- (60) Giovannetti, G.; Khomyakov, P. A.; Brocks, G.; Karpan, V. M.; van den Brink, J.; Kelly, P. J. Doping Graphene with Metal Contacts. *Phys. Rev. Lett.* **2008**, *101*, 026803.
- (61) Kuroda, M. A.; Tersoff, J.; Martyna, G. J. Nonlinear Screening in Multilayer Graphene Systems. *Phys. Rev. Lett.* **2011**, *106*, 116804.
- (62) Vlassiuk, I. V.; Stehle, Y.; Pudasaini, P. R.; Unocic, R. R.; Rack, P. D.; Baddorf, A. P.; Ivanov, I. N.; Lavrik, N. V.; List, F.; Gupta, N.; Bets, K. V.; Yakobson, B. I.; Smirnov, S. N. Evolutionary selection growth of two-dimensional materials on polycrystalline substrates. *Nat. Mater.* **2018**, *17*, 318–322.